High resolution MRI of uveal melanoma using a microcoil phased array at 7 Tesla

which was published in:

1*NMR Biomed.* **26**, 1864–1869 (2013)
doi:10.1002/nbm.3041.

High resolution MRI of uveal melanoma using a microcoil phased array at 7 Tesla

J.W.M. Beenakker[1,2], G.A. van Rijn[2], G.P.M. Luyten[2], and A.G.Webb[1]

[1]C.J.Gorter Center for High Field MRI, Department of Radiology, [2]Department of Opthalmology

Leiden University Medical Center, Leiden, The Netherlands.

Corresponding author:

Jan-Willem Beenakker,

Departments of Opthalmology and Radiology

Leiden University Medical Center,

Albinusdreef 2, Leiden 2333 ZA,

Key words: high resolution ocular MRI, optical biometry, uveal melanoma, microcoil array, motion suppression.

Abbreviations

bSSFP	balanced steady state free precession
FOV	field-of-view
OCT	optical coherence tomography
PCI	partial coherence laser interferometry
PLA	poly-lactic acid
RF	radiofrequency
SAR	specific absorption rate
SNR	signal-to-noise ratio
TCP	transmission control protocol

Abstract

High field MRI is a promising technique for characterizing ocular tumours both in vivo and after enucleation. For in vivo imaging at 7 Tesla a dedicated three-element microcoil array was constructed as a high sensitivity receive-only device. Using a dedicated blink/fixation protocol, high resolution in vivo images could be acquired within three minutes in volunteers and patients with no requirement for post-acquisition image registration. Quantitative measures of axial length, aqueous depth and lens thickness in a healthy volunteer were found to agree well with standard ocular biometric techniques. In a patient with uveal melanoma, in vivo MRI gave excellent tumour/aqueous body contrast. Ex-vivo imaging of the enucleated eye showed significant heterogeneity within the tumour.

Introduction

High-resolution magnetic resonance imaging (MRI) is developing as a promising tool for ocular imaging in terms of detailed structures (1-5), pathological conditions (6-13), non-invasive blood flow measurements (14, 15), natural ageing (16-19), and potentially for intraocular lens surgery (19). The versatility of MRI combined with the fact that it is a non-contact technique, make it a valuable additional imaging modality to, for example, optical coherence tomography (OCT) and ultrasound. Recent fMRI studies have, for example, shown a change in blood flow of the retina under different physiological conditions(Peng e.a. 2011; Nasim Maleki e.a. 2011b; N. Maleki e.a. 2011a; Zhang e.a. 2011). An additional benefit of MRI is its ability to image within dense tissues, such as uveal melanoma (20), which is not possible with OCT or ultrasound due to the limited penetration depth. In terms of improving the spatial resolution even further, the major development areas are in radiofrequency (RF) coil design and high magnetic fields. These result in a higher signal-to-noise ratio (SNR), which in turn translates to higher spatial resolution and/or more rapid imaging sequences to mitigate the effects of eye movement.

Although many studies at 1.5T and 3T use the standard head coil for imaging, significantly improved image quality can be realized by using specialized receive coils. Single receive surface coils (21), with diameters typically ~5 cm, are commercially available from all major vendors. Four channel receive-only eye coils are also commercially available for 3T scanners. Research groups have designed more elaborate coil arrays: for example, Minalga et al. (22) have constructed a 20-coil receive array specifically for imaging the optic nerve at 3T. In this configuration, two 6.35 x 7 cm oval loops covered the eyes, with the remaining circular loops distributed over the head.

Initial MRI studies on a whole body human 7 Tesla scanner (4, 19, 23) have shown the possibility of detailed imaging of the internal structures, such as the posterior ciliary vessels. Since the images are highly motion-sensitive, studies at 7T have so far acquired several low

SNR images very rapidly, followed by image registration and subsequent co-addition of scans (4, 23). These studies used either a commercial 5 cm diameter receive-only surface coil, with a quadrature volume coil used for transmission, or a 2 x 2.3 cm single loop oval coil. Recently, a six-channel transceiver array coil has been constructed for 7 Tesla, with three elements for each eye (24). T_1- and T_2-weighted images were acquired with voxel sizes of 0.5 x 0.5 x 3 mm. (25).

The major issue with obtaining high resolution images in vivo is the motion of the eye (26). As discussed in Fanea and Fagan (6) the average time between blinks is 4 s in women and 2.8 s in men, with the duration of each blink varying from 0.3 to 0.4 s (27). Berkowitz et al. (REF) instructed subjects to focus on a fiber optic line with blinking cued every 15 s and image acquisition being triggered by the cued blinking. Zhang et al. (1) used an eye tracker to measure eye motion and have suggested cued blinking every 8 s. Using this paradigm Zhang et al. were able to acquire very high resolution single slice images which clearly showed the retinal layers. The aim in this current study is to develop a working clinical protocol at 7 Tesla that can be used for patients to produce high-resolution images of eye tumours within a rapid scanning time, with a spatial resolution that allows accurate distances to be measured between features within the eye, and which need no subsequent image processing so that image quality can be evaluated in real time by a consulting ophthalmologist. The first component was to develop a high-sensitivity three-channel microcoil array which yields sufficient SNR to image the eye with one scan. A blinking scheme adapted from that of Zhang et al. (1) allowed scans of up to three minutes duration to be acquired without visible eye-motion artefacts. Quantitative comparisons of eye geometry measurements with standard ocular biometric measures were performed for validation. Finally, these techniques were to image in-vivo the internal structure of uveal melanomas and compare them with high resolution images taken after enucleation of the eye.

Experimental.

Construction of a three-channel receive eye-coil

By using a volume coil for transmission and a surface coil array for receiving, figure 1A, the benefits of homogeneous excitation and sensitive reception are combined. In addition, the smaller field-of-view (FOV) of the surface coil array reduces the scan time require for a given spatial resolution, which is a key issue in ocular imaging.

Each loop in the array is made of 1 mm-diameter silver wire and has a diameter of 28 mm. The coil is segmented by two non-magnetic capacitors (8.2 pF, Series C, American Technical Ceramics). In parallel with one of these capacitors a circuit consisting of a non-magnetic PIN-diode (MA4P7441F-1091T , M/A-COM) and 30 nH inductor enables active detuning of each of the receive coils during transmit. The coupling between the individual loops in the array is minimized by overlapping each element in a “Venn-diagram” geometry. Each channel has a separate cable trap consisting of a parallel LC circuit ~1 cm from the coil, directly after which the ground connections of the three loops are soldered together. An additional bazooka-type balun is placed 14 cm from the coil to minimise the coupling between the transmit and the receive coil. A dedicated housing was printed (3D Touch, Bits From Bytes) in poly-lactic acid (PLA) to facilitate reproducible positioning of the coil on each subject. A small mirror allows the subject to watch, with the non-imaged eye, a projector screen inside the bore of the 7 Tesla whole-body MRI.

MR imaging

All MRI experiments were performed on a Philips Achieva 7 Tesla whole body magnet. The transmit coil was a quadrature birdcage ((Nova Medical Inc., Wilmington, MA, USA), which has active detuning. All protocols were approved by the local medical ethics committee, and informed consent was obtained from all volunteers and patients.

The main aim of our current project is high resolution imaging of eye tumours in vivo, and to determine tumour size, location and presence of extra-scleral growth, since these are important clinical features in determining the prognosis for uveal melanomas (20). To this end the parameters that best nulled the signal from the surrounding aqueous body were used, and these were derived from initial work by Richdale et al. (23). MR images were acquired using a three-dimensional inversion recovery turbo gradient echo technique with the following parameters: TS=3000ms, TR/TE/flip-angle 2.5/4.55ms/16°, TFE-factor=92, FOV=40x46x38mm^3, spatial resolution 0.5 x 0.5 x 1.0mm^3, one signal average, 2:50min scan time. Saturation slabs were placed around the imaging field-of-view to reduce the effects of aliasing in the phase encoding directions.

After acquisition of the scans, the three-dimensional data set was rotated to determine the visual axis of the eye. A line plot of image intensity was then drawn along this axis to determine the axial length for comparison with ocular biometry.

In addition to volunteer scans, data sets have been obtained from patients with uveal melanomas, which is the most commonly found primary intra-ocular malignant tumour in adults (20). Although the melanoma can affect any part of the uveal tract, the tumour preferentially affects the choroid, while iris and ciliairy body melanomas are less frequently seen. The patient whose images are shown in this paper had developed a large subretinal mass with secondary retinal detachment and consequent visual loss, a complication commonly found in choroidal melanoma.

Subject preparation and gaze fixation

To aid the subject in keeping the imaged eye closed during scanning, a small piece of tape is placed over their eyelid (2). Magnetic susceptibility effects are particularly problematic at high field using gradient echo techniques, and previous researchers (23) have found that placing a wetted-gauze on top of the closed eyelid helps to minimize these image distortions. Different fixation methods were investigated to find the optimal balance between patient comfort and artefacts resulting from eye movement. A Maltese cross is commonly used as a fixation target: however, approximately every 20 to 30 seconds subjects temporarily lost their fixation, resulting in significant motion artefacts in the 3 minute scan. Projecting a small (8x11 cm^2) film onto a white screen, placed at the back of the magnet at a distance of 1.3 m from the mirror on the head coil, gave similar results in terms of image artefact, but was more convenient for the subject. However, although working well for emmetropic volunteers, this method would not be suitable for subjects with impaired vision or high refractive errors, since focussing on small images (without glasses or contact lenses) is challenging in these cases.

In order to deal with this loss of fixation due to blinking, the approach of Zhang et al. (1) for cued blinking triggers was adapted. Cued blinking, introduced every three seconds, significantly reduced motion artefacts in the images in which the delay of approximately 1.5 seconds between successive imaging shots provides a small time window in which the subject could relax their gaze without causing motion artefacts. The period of three seconds is close to the natural blinking period (27), and enabled rapid and efficient imaging to be performed. By linking the projection system to the MRI computer, using a transmission control protocol (TCP) socket communication, the subject receives synchronised visual instructions on when to blink, as shown in figure 2. This fixation method not only resulted in minimal motion artefacts, but the subjects also evaluated this method as much more comfortable compared to the alternatives of watching the movie or a single continuous fixation target.

Ocular biometry

The Lenstar LS 900 system (Haag-Streit AG, Koeniz, Switzerland) was used to perform non-contact axial length measurements on healthy volunteers. This technique is based upon the principles of partial coherence laser interferometry (28). Five separate measurements of axial length, aqueous depth and lens thickness were averaged and compared to the MRI data projected along a line profile through the centre of the lens.

Ultrasound

Ultrasound images of the tumour patient were obtained using a Lin 50 UBM probe (Quantel Medical Aviso, France). The transducer frequency was 50 MHz, with a linear transducer exploration width of 16 mm , focus 9 to 11 mm, axial resolution 35 μm and lateral resolution 60 μm (data supplied by manufacturer).

Ex vivo imaging of enucleated eyes from tumour patients

One day after in vivo imaging of the eye, in selected tumour patients, the enucleated eye was made available within three hours post-surgery for ex vivo high resolution MRI. Since rapid histological analysis of the eye should be performed post-enucleation, the MRI protocol was limited in time to ~1 hour. After enucleation, the eye was immersed in a 50 ml tube filled with a perfluorinated liquid (Fomblin, Solvay Solexis), which prevents dehydration and has no background MR signal. The sample was imaged on a 7T Bruker Pharmascan 70/16 scanner, using a quadrature birdcage coil (outer diameter 89 mm, inner diameter 39 mm), and BGA90S gradients (inner diameter 90 mm, maximum gradient strength 750 mT/m, maximum slew rate 7500 mT/m/s). A three dimensional triple echo gradient echo sequence was run with the following parameters: TR/TE1/TE2/TE3/flip-angle 31/6/15/24 ms/20°, FOV

30 x 30 x 30 mm^3, spatial resolution 0.12 x 0.12 x 0.12 mm^3, two signal averages, 67 minute scan time.

Results

Coil characterisation

The S_{11} measurements of the individual channels, one of which is shown in Figure 3, shows the effect of loading on the coil: the Q value drops from 150 unloaded to 100 loaded, with minimal frequency shift meaning that the coil does not have to be tuned to individual patients. The effectiveness of the detuning circuit is also shown in Figure 3, where the S_{11} at the resonance frequency of 298.1 MHz is essentially the noise floor of the measurement. Before every excitation, the MRI hardware verifies if a DC current can pass through each of the three channels of the coil. If any of the components break or if the PIN-diode fails to switch, no current is measured and the scan is automatically aborted. The detuning circuit has a broad resonance peak to assure effective detuning on a wide frequency range. The use of the commercial head coil for transmit allows the calibrated specific absorption rate (SAR) settings of the commercial head coil to be used. The safety of the set-up was further verified by running a SAR-limited scans on a phantom (a hollow plastic mould in the shape of the human head filled with gel with tissue mimicking values of conductivity and permittivity), which showed no increase in temperature as measured by MRI-compatible optical fibre temperature sensors (Opsens, Montreal, Canada).

MRI scans of healthy controls

Figure 4 shows that the intermittent blinking paradigm enables the acquisition of 3D images of the eye with minimal motion artefacts, which otherwise show as areas of inhomogeneous “speckle” within the vitreous body or distinct “ghosts” of the outline of the eye. The images

show that the penetration depth of the coil array is sufficient to cover the back of the eye, allowing anatomical structures of the eye, such as the lens, retina, cornea and optic nerve to be visualized.

The geometric accuracy of the MRI data was verified by comparing it with an optical biometry measurement using partial coherence laser interferometry (PCI), Figure 5. PCI can achieve accuracy on the order of 0.02 mm, whereas the accuracy of the MRI measurements is approximately equal to the voxel resolution of 0.5 mm. Figure 5B shows a line profile from the MR image along the optical axis of a healthy volunteer wearing contact lenses. The length measurements performed on the MRI data are in good agreement with the PCI measurements. This confirms the observations in previous studies which have also shown good agreement between imaging modalities in the anterior part of the eye (3, 19). The current MRI setup, however, also allows for 2D dimensional measurements in the posterior part of the eye, such as ocular circumference, to be made, which is not possible with OCT due to its limited penetration depth or with PCI as it can only perform one dimensional on-axis measurements.

Imaging a patient with uveal melanoma

One of the most promising potentials of MRI in clinical opthalmology is the characterisation of uveal melanoma. Ultrasound is able to give a rough estimation of the melanoma size, but due to its limited penetration depth, little information on the internal structure of the melanoma can be obtained. MRI has recently been used to study uveal melanoma in different animal models(Braun e.a. 2007; Krause e.a. 2002). MRI is able not only to show the internal structure of the melanoma, but may also be able to show if the melanoma has grown through the sclera, which can lead to rapid metastasis throughout the body. Different images from the patient with uveal melanoma are shown in Figure 6. Ultrasound, Figure 6A, shows a large subretinal mass, but no substructures within the mass. The in vivo MRI scan, Figure

6B, shows more internal structure of the tumour, with better shape delineation, accompanied by a commonly seen retinal detachment secondary to the tumours growth. Figures 6 C is a zoomed view of the tumour, which shows the heterogeneity within the structure. Figures 6D and E show images from the 7T Pharmascan MRI system of the enucleated eye. The highly inhomogeneous structures inside the melanoma can be seen on the T_2^*-weighted scans.

Discussion

A dedicated three-channel microcoil array combined with a blink/cue imaging protocol makes it possible to image the eye with a scan time of less than three minutes without visible motion artefacts. In terms of coil sensitivity, the smaller the coils the higher the intrinsic sensitivity. However, the lower limit has been suggested to be ~2.5 cm (29), and the diameter of the individual loops of the array was chosen to be sufficient to enable signals to be picked up from the back of the eye. Three coils is the maximum number that can be decoupled via overlap.

Whereas previous 7 T scan protocols used offline registration and combination of the individual images (4, 23), this current imaging method has sufficient SNR to acquire the images in a single scan, which is an important feature in routine clinical use. Since the protocol is aimed towards in vivo tumour imaging, some in-plane spatial resolution was sacrificed in order to reduce the slice thickness to 1 mm due to the three-dimensional tumour inhomogeneity. The in-plane resolution is higher than typically acquired clinically, but is not as high as has been reported by Zhang et al. (1) in their study of laminar-specific imaging, in which an impressive 0.1 x 0.2 x 2 mm single slice was acquired using a balanced steady state free precession sequence (bSSFP) with partial Fourier encoding. At 7 Tesla it is challenging to acquire bSSFP images over the entire eye given the higher image distortion and banding arising from magnetic field inhomogeneities, as well as the presence of the tumour.

Nevertheless, sequence optimization in terms of SNR efficiency is one area that warrants further investigation.

The spatial resolution (in terms of voxel volume) of in vivo MRI is approximately two orders of magnitude poorer than that obtainable ex vivo. Nevertheless, the geometrical shape of the tumour as seen in the ex-vivo scans is well represented by the in vivo scans. Parameters to optimize the contrast within the tumour have not yet been investigated, but a longer echo time, for example, can be anticipated to introduce more contrast from the internal structure of the tumour, as indicated by the ex vivo scans of the enucleated eye, at the price of reduced SNR. In turn, the ex vivo scans are much poorer spatial resolution than can be obtained using histology. However, using an animal magnet, Krueger et al. (13) performed high resolution (78 x 78 x 500 μm) ex-vivo imaging at 7 Tesla in a case of uveal melanoma, where MR microscopy of the tumour showed very good correlation with its histology. The path between pathology and direct visualization in vivo therefore appears to be promising. Future studies could also employ more advanced in vivo MRI methods used in tumour imaging such as perfusion imaging(Sugahara e.a. 2000; Weber e.a. 2006; Hu e.a. 2012)(Yoo e.a. 2013), manganese-enhanced MRI(Braun e.a. 2007; Krause e.a. 2002) and dynamic contract enhanced (DCE) MRI(Buckley e.a. 1997; PADHANI e.a. 2000; Laarhoven e.a. 2003; Yaligar e.a. 2012) to study tumour morphology and progression.

Acknowledgements

The authors would like to thank W.M. Teeuwisse for his help with setting up the initial experiments, L. van der Weerd and E. Suidgeest for the help with and use of the Bruker Pharmascan, J. Smink (Philips Healthcare) for help with the TCP socket communication, and M. Versluis for the preparation of the enucleated eye. This work was supported in part by

Agentschap NL (an agency of the Dutch Ministry of Economic Affairs), as part of the EUREKA/NPV project.

References

1. Zhang Y, Nateras OS, Peng Q, Kuranov RV, Harrison JM, Milner TE, Duong TQ. Lamina-specific anatomic magnetic resonance imaging of the human retina. Invest Ophthalmol Vis Sci 2011;52(10):7232-7237.

2. Bert RJ, Patz S, Ossiani M, Caruthers SD, Jara H, Krejza J, Freddo T. High-Resolution MR Imaging of the Human Eye 2005. Academic Radiology 2006;13(3).

3. Koretz JE, Strenk SA, Strenk LM, Semmlow JL. Scheimpflug and high-resolution magnetic resonance imaging of the anterior segment: a comparative study. J Opt Soc Am A Opt Image Sci Vis 2004;21(3):346-354.

4. Christoforidis JB, Wassenaar PA, Christoforidis GA, Ho VY, Knopp MV, Schmalbrock PM. Retrobulbar vasculature using 7-T magnetic resonance imaging with dedicated eye surface coil. Graefes Arch Clin Exp Ophthalmol 2012.

5. Ettl A, Zwrtek K, Daxer A, Salomonowitz E. Anatomy of the Orbital Apex and Cavernous Sinus on High-Resolution Magnetic Resonance Images. Survey of Ophthalmology 2000;44(4).

6. Fanea L, Fagan AJ. Review: magnetic resonance imaging techniques in ophthalmology. Mol Vis 2012;18.

7. Kolk A, Stimmer H, Klopfer M, Wolff K-D, Hohlweg-Majert B, Ploder O, Pautke C. High resolution magnetic resonance imaging with an orbital coil as an alternative to computed tomography scan as the primary imaging modality of pediatric orbital fractures. J Oral Maxillofac Surg 2009;67(2).

8. Lemke A-J, Alai-Omid M, Hengst SA, Kazi I, Felix R. Eye imaging with a 3.0-T MRI using a surface coil – a study on volunteers and initial patients with uveal melanoma. Eur Radiol 2006;16(5).

9. Mafee MF, Rapoport M, Karimi A, Ansari SA, Shah J. Orbital and Ocular Imaging Using 3- and 1.5-T MR Imaging Systems. 2005;15(1).

10. Trick GL, Edwards PA, Desai U, Morton PE, Latif Z, Berkowitz BA. MRI retinovascular studies in humans: research in patients with diabetes. NMR Biomed 2008;21(9).

11. Townsend KA, Wollstein G, Schuman JS. Clinical application of MRI in ophthalmology. NMR Biomed 2008;21(9):997-1002.

12. Bahn MM, Gordon RE, Wippold FJ, Grand MG. Findings of retinitis on gadolinium-enhanced turbo fluid-attenuated inversion recovery images. Retina 1998;18(2):164-168.

13. Spierer O, Ben SL, Leibovitch I, Kesler A. MRI demonstrates restricted diffusion in distal optic nerve in atypical optic neuritis. J Neuroophthalmol 2010;30(1):31-33.

14. Li Y, Cheng H, Duong TQ. Blood-flow magnetic resonance imaging of the retina. NeuroImage 2008;39(4).

15. Peng Q, Zhang Y, Nateras OS, van Osch MJ, Duong TQ. MRI of blood flow of the human retina. Magn Reson Med 2011;65(6):1768-1775.

16. Strenk SA, Semmlow JL, Strenk LM, Munoz P, Gronlund-Jacob J, DeMarco JK. Age-related changes in human ciliary muscle and lens: a magnetic resonance imaging study. Invest Ophthalmol Vis Sci 1999;40(6):1162-1169.

17. Strenk SA, Strenk LM, Guo S. Magnetic resonance imaging of aging, accommodating, phakic, and pseudophakic ciliary muscle diameters. J Cataract Refract Surg 2006;32(11):1792-1798.

18. Sheppard AL, Evans CJ, Singh KD, Wolffsohn JS, Dunne MC, Davies LN. Three-dimensional magnetic resonance imaging of the phakic crystalline lens during accommodation. Invest Ophthalmol Vis Sci 2011;52(6):3689-3697.

19. Richdale K, Sinnott LT, Bullimore MA, Wassenaar PA, Schmalbrock P, Kao CY, Patz S, Mutti DO, Glasser A, Zadnik K. Quantification of age-related and per diopter accommodative changes of the lens and ciliary muscle in the emmetropic human eye. Invest Ophthalmol Vis Sci 2013;54(2):1095-1105.

20. Spagnolo F, Caltabiano G, Queirolo P. Uveal melanoma. Cancer Treat Rev 2012;38(5):549-553.

21. Georgouli T, James T, Tanner S, Shelley D, Nelson M, Chang B, Backhouse O, McGonagle D. High-resolution microscopy coil MR-Eye. Eye (Lond) 2008;22(8):994-996.

22. Minalga E, Rose J, Choi SE, Jeong EK, Kholmovski E, Vijayakumar S, Parker D, Hadley R. A 20-channel coil for improved magnetic resonance imaging of the optic nerve. Concepts Magn Reson Part B Magn Reson Eng 2011;39B(1):26-36.

23. Richdale K, Wassenaar P, Teal Bluestein K, Abduljalil A, Christoforidis JA, Lanz T, Knopp MV, Schmalbrock P. 7 Tesla MR imaging of the human eye in vivo. J Magn Reson Imaging 2009;30(5).

24. Graessl, A., Schwerter, M., Muhle, M., Rieger, J., Oezerdam, C., Ok, A., Santor, D., Lysiak, D., Stachs, O., Langner, S., Krueger, P. C., and Niendorf, T. Design, evalutaion and application of a six-channel transceiver array tailored for in vivo human eye imaging at 7.0T [abstract]. In: Int.Soc.Magn.Reson.Med., Salt Lake City, UT, USA, 2013. p2747.

25. Krueger PC, Stachs O, Hadlich S, Falke K, Erbersdobler A, Hosten N, Langner S. MR Microscopy of the human eye at 7.1 T and correlation with histopathology-proof of principle. Orbit 2012;31(6):390-393.

26. Berkowitz BA, McDonald C, Ito Y, Tofts PS, Latif Z, Gross J. Measuring the human retinal oxygenation response to a hyperoxic challenge using MRI: eliminating blinking artifacts and demonstrating proof of concept. Magn Reson Med 2001;46(2):412-416.

27. Yarbus AL. Eye movements during fixation on stationary objects and saccidic eye movements. In: Haigh B, RIggs LA, editors. Eye movements and vision. New York: Plenum Press; 1967. 103-146.

28. Cruysberg LPJ, Doors M, Verbakel F, Berendschot TTJM, De Brabander J, Nuijts RMMA. Evaluation of the Lenstar LS 900 non-contact biometer. British Journal of Ophthalmology 2009;94(1).

29. Kumar A, Edelstein WA, Bottomley PA. Noise figure limits for circular loop MR coils. Magn Reson Med 2009;61(5):1201-1209.

Figures

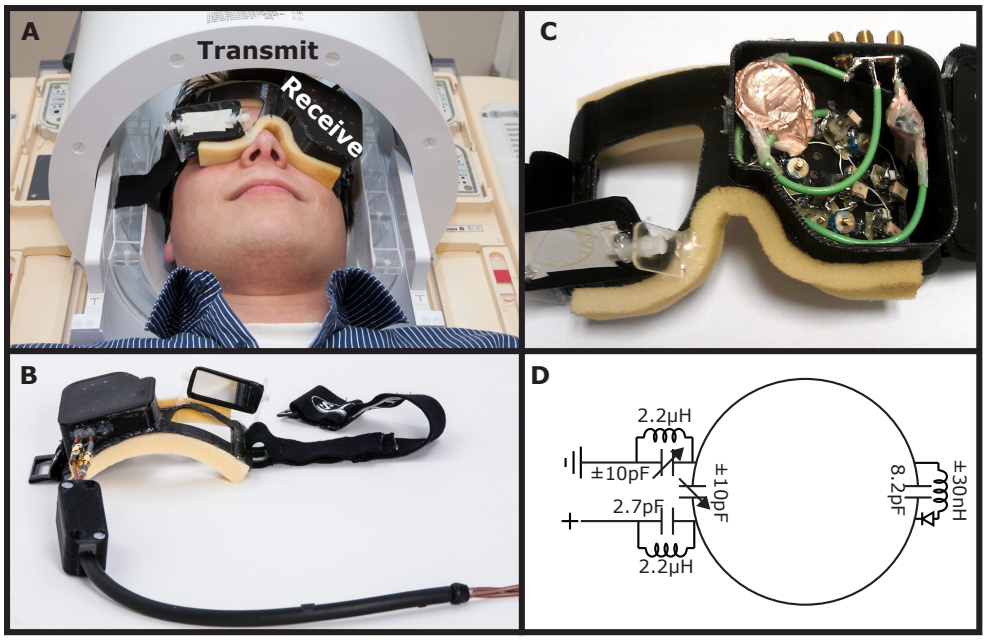

Figure 1. The design of the 3-channel eye coil. A) Physical integration with the transmit quadrature head coil. B) The electronics are mounted in a 3D printed housing. A small, adjustable, mirror allows the subject to look outside the bore of the MRI onto a projection screen. (D) Schematic of the electronics of each element of the three-channel eye-coil. Each channel has a balanced matching network and an active detuning circuit.

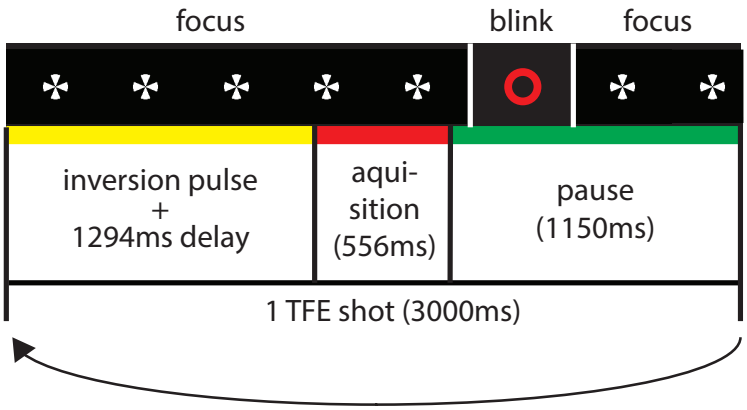

Figure 2: Acquisition scheme to minimize eye-motion artefacts. The inversion recovery three-dimensional gradient echo sequence consists of three parts: the inversion pulse followed by a delay 1280 ms, rapid acquisition of 76 k-space lines, and a pause of 1150 ms before the next inversion pulse is given. During the scan, the subject is asked to focus on a Maltese cross. 100 ms after each acquisition block the subject is asked to quickly blink their eyes, which is signalled by the projection of a red circle for 200 ms.

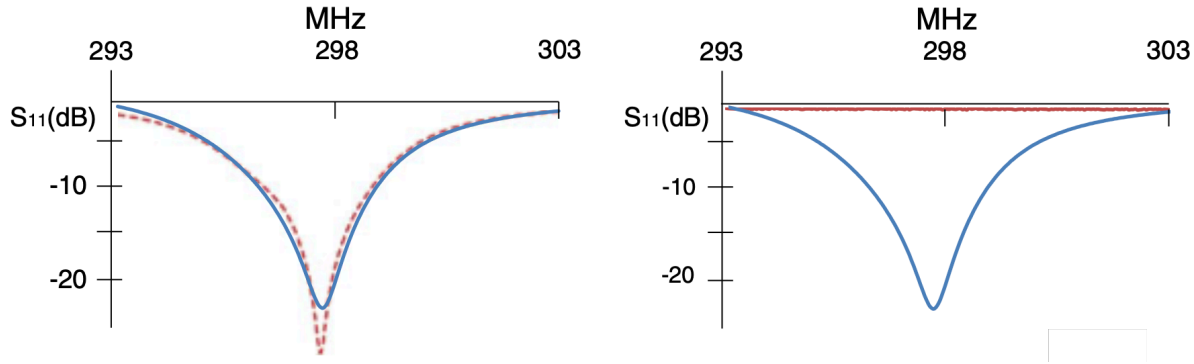

Figure 3: Characteristics of the three channel receive coil. (left) S_{11} measurements of the unloaded (dotted line) and loaded (solid line) conditions. (right) S_{11} measurements showing the effects of the detuning voltage applied to the diodes on the array.

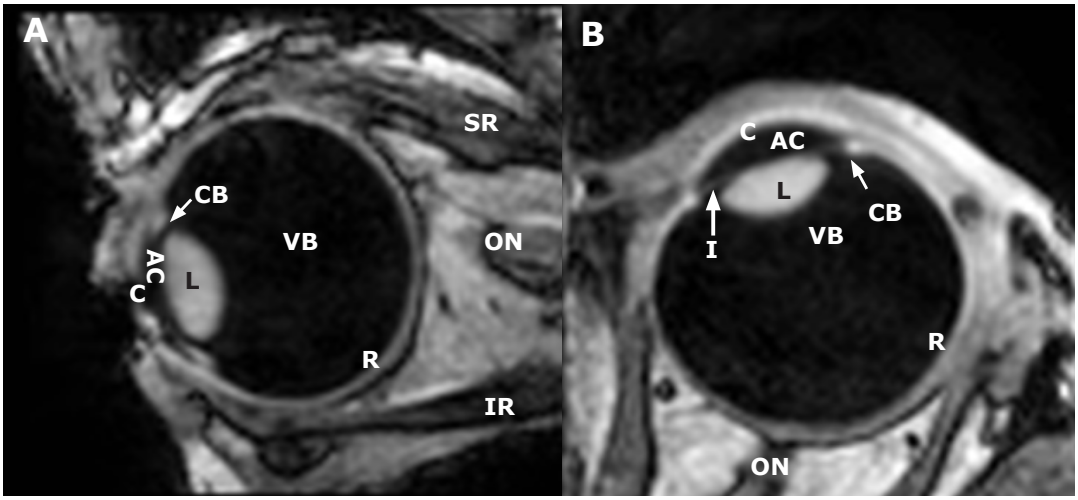

Figure 4: Sagittal (A) and transverse (B) image showing the different anatomical features of the eye in a healthy volunteer: Lens (L), cornea (C), anterior chamber (AC), ciliary body (CB), vitreous body (VB), retina and sclera (R), optic nerve (ON), inferior rectus (IR) and superior rectus (SR).

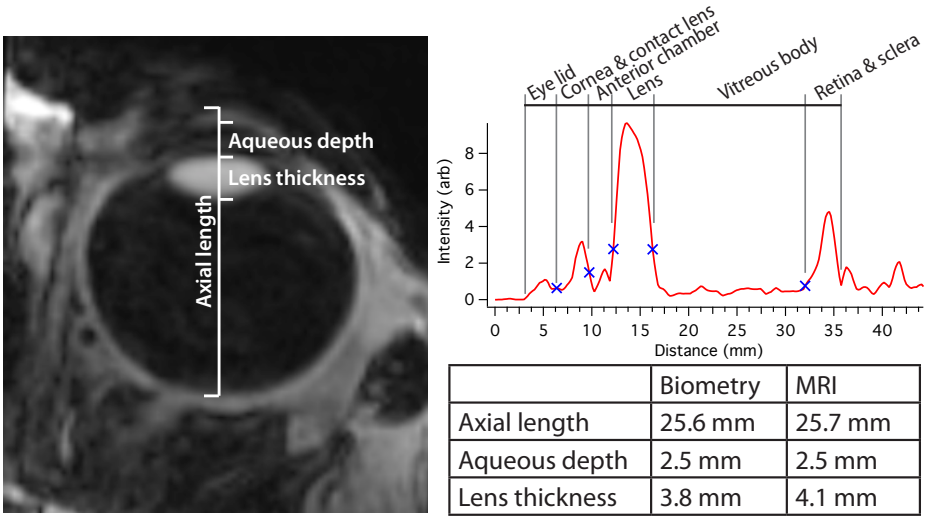

	Biometry	MRI
Axial length	25.6 mm	25.7 mm
Aqueous depth	2.5 mm	2.5 mm
Lens thickness	3.8 mm	4.1 mm

Figure 5: Comparison of axial length measurements: A) Transverse slice through the optical plane showing the optical axis. B) Line profile through the optical axis showing the various anatomical features. C) Comparison between three length measurements made using PCI (Lenstar) and MRI.

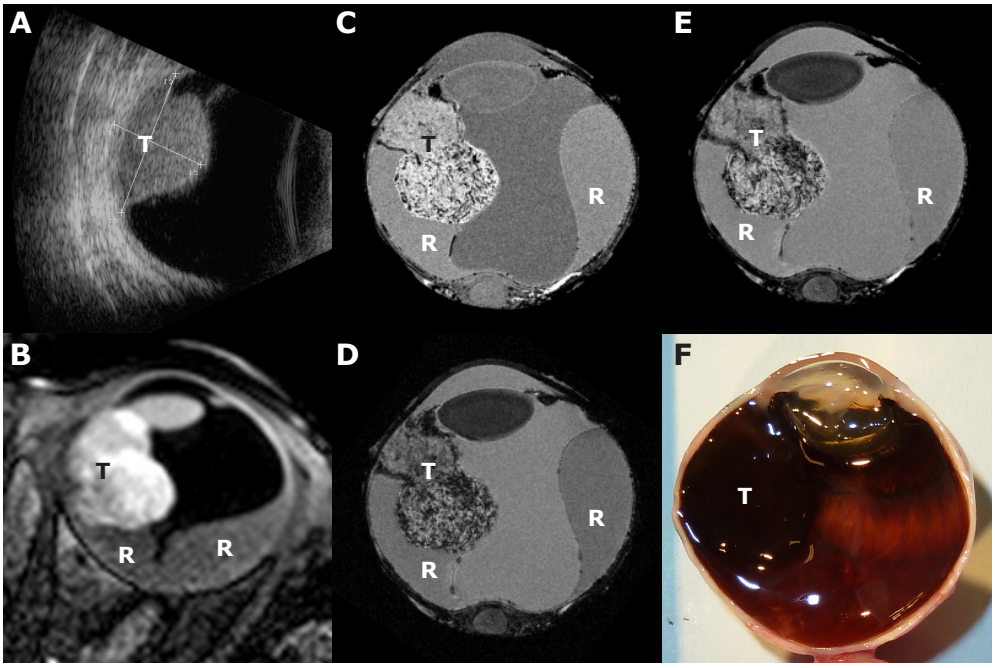

Figure 6: Images from a patient with an uveal melanoma**.** In vivo ultrasound (A) and MRI (B) images of an uveal melanoma (T) in the left eye. The MRI also shows a detached retina (R), a common feature of uveal melanoma. (C) Zoomed view of the tumour showing the signal heterogeneity within the structure. (D,E) Post-enucleation high resolution scans of the eye. (D) TE = 24 ms, (E) co-addition of three echoes at TE=6, 15 and 24 ms. The images show a rich structure inside the melanoma. F) Optical cross-section of the eye after the *ex vivo* MRI scan showing the melanoma in black.